

Effects of Dynamo-Generated Large-Scale Magnetic Fields on the Surface Gravity (*f*) Mode

RAJESH MONDAL¹ AND NISHANT K. SINGH¹

¹*Inter-University Centre for Astronomy & Astrophysics, Post Bag 4, Ganeshkhind, Pune 411007, India*

ABSTRACT

By modelling the upper layers of the Sun in terms of a two-layer setup where a free-surface exists within the computational domain, we numerically study the interaction between the surface gravity, or the fundamental (*f*) mode, and the magnetic fields. Earlier such works were idealized in the sense that the static magnetic fields were imposed below the photosphere, i.e., the free-surface, to detect signatures of sub-surface magnetic fields and flows on the *f*-mode. In this work, we perform three-dimensional (3D) numerical simulations where the interior fluid below the photosphere is stirred helically at small scales, thus facilitating an α^2 -dynamo. This allows us to investigate how these self-consistently generated large-scale magnetic fields influence the properties of the *f*-mode. We find that when the magnetic fields saturate near the equipartition values with the turbulent kinetic energy of the flow, the *f*-mode is significantly perturbed. Compared to the non-magnetic case, or the kinematic phase of the dynamo when fields are too weak, we note that the frequencies and the strengths of the *f*-mode are enhanced in presence of saturated magnetic fields, with these effects being larger at larger wavenumbers. This qualitatively confirms the earlier findings from observational and numerical works which reported the *f*-mode strengthening due to strong sub-surface magnetic fields.

Keywords: Helioseismology (709), Solar magnetic fields (1503), Magnetohydrodynamical simulations (1966)

1. INTRODUCTION

Techniques of helioseismology, especially those involving the acoustic or the *p*-modes, have been extremely useful in measuring the interior properties of the Sun (Christensen-Dalsgaard 2002; Gizon & Birch 2005). The Sun also supports the fundamental, or the *f*-mode whose eigenfunction lies only close to the photosphere. Due to its simplistic dispersion relation which is not sensitive to the background thermodynamics, the *f*-mode is often considered to be of lesser diagnostic value. However, a number of earlier works suggest that the *f*-modes can be significantly perturbed in presence of the magnetic fields (Chandrasekhar 1961; Roberts 1981; Miles & Roberts 1989, 1992; Miles et al. 1992; Cally & Bogdan 1997; Erdélyi et al. 2005; Hanasoge et al. 2008; Parchevsky & Kosovichev 2009; Singh et al. 2014; Singh et al. 2015; Kiefer et al. 2017; Tripathi & Mitra 2022).

In addition to these studies, several observational works have explored the use of the *f*-mode as a diagnostic of sub-surface magnetic fields. For example, Thompson (2006) an-

alyzed frequency shifts of both *p*- and *f*-modes and inferred the presence of subsurface magnetic fields with strengths of order 500 G at depths of approximately 5 Mm. Singh et al. (2016) reported a systematic strengthening of the *f*-mode one to two days before the emergence of active regions (AR), based on their analysis on the data from the Helioseismic and Magnetic Imager aboard the Solar Dynamics Observatory. Their findings were later confirmed by Waidele et al. (2023) using a different technique involving the Fourier–Hankel analysis. These studies signify the importance of the *f*-mode as a useful tool in predicting the emergence of sunspots or AR, and this topic remains an area of active research; see also Korpi-Lagg et al. (2022); Kasapis et al. (2024, 2026).

Properties of the *f*-mode in presence of the magnetic fields have also been studied extensively in various numerical works. For example, Daifallah et al. (2011); Felipe et al. (2012) studied the scattering of *f*-mode by thin magnetic flux tubes and found that the amplitude of the scattered wave approximately scales with the magnetic flux of the flux tubes. Singh et al. (2015) through their piecewise isothermal setups in 2D studied the properties of *p*- and *f*-modes by considering a variety of magnetic configurations. When nonuniform magnetic fields were used in a similar setup, it was found that the *f*-mode fans out in the diagnostic $k\omega$ diagrams, and it dis-

plays strengthening as compared to the f -mode strengths obtained in the purely hydrodynamic cases (Singh et al. 2014, 2020). They also demonstrated that the f -mode amplitude sensitively depends on the depth of magnetic field concentrations, further highlighting its potential for mapping subsurface magnetic fields.

Extending these works further, Kishore et al. (2024) performed more realistic convection simulations in 3D, and in qualitative agreement to earlier reports on the f -mode strengthening, they found that when strong magnetic fields are imposed just beneath the photosphere, the f -mode amplitudes become significantly larger compared to the cases with either weak or no magnetic fields. What is common in all these numerical works is that the magnetic fields are imposed and their strengths are quite strong compared to the local equipartition values.

In this work, we relax this assumption of an artificially imposed magnetic fields by exciting an α^2 dynamo (Brandenburg & Subramanian 2005) through a helical forcing of the fluid below the free-surface. This allows us to study the interaction between the f -mode and a self-consistently generated equipartition-level large-scale magnetic fields below the photosphere.

In Section 2, we describe the model and numerical setup used in this study. Section 3 outlines the methodology for analysing the f -mode. In Section 4, we present our results by exploring the effects of self-sustained large-scale magnetic fields on the f -mode. We conclude in Section 5.

2. MODEL AND NUMERICAL SETUP

2.1. Model

We aim to investigate the influence of dynamo-generated large-scale magnetic fields on high-degree f -modes, which remain confined near the solar surface and are therefore sensitive to sub-surface magnetic fields. For this purpose, it is sufficient to consider a Cartesian box filled with conducting fluid, which can be regarded as a local representation of a small region of the solar surface. This approach allows us to avoid the numerical complexity of a spherical domain and focus on the underlying physical processes.

We consider a Cartesian coordinate system with unit vectors \mathbf{e}_x , \mathbf{e}_y , and \mathbf{e}_z along the x , y , and z directions, respectively. The system consists of a Cartesian box of dimensions L_x , L_y , and L_z along the \mathbf{e}_x , \mathbf{e}_y , and \mathbf{e}_z directions, respectively, where \mathbf{e}_z denotes the vertical direction (corresponding to the radial direction in the solar context) and \mathbf{e}_x , \mathbf{e}_y the horizontal directions. For our purpose, we assumed $L_z \ll L_x, L_y$, signifying that the system is significantly thinner in the vertical direction compared to the horizontal directions so that we can work in the framework of parallel plane approximation. For reference, we have added a schematic

diagram (2D cross-section) of the model is shown in the top panel of Figure 1.

Gravity acts along the $-\mathbf{e}_z$ direction, and its magnitude is denoted by $g (> 0)$. Given the small vertical extent of the domain, we have assumed gravity to be constant. This model also includes an interface located at $z = 0$, which divides the domain into two subdomains, a lower layer of thickness L_{zd} and an upper layer of thickness L_{zu} . We have assumed $L_{zd} = 9L_z/10$ and $L_{zu} = L_z/10$ for all the simulations presented in this paper.

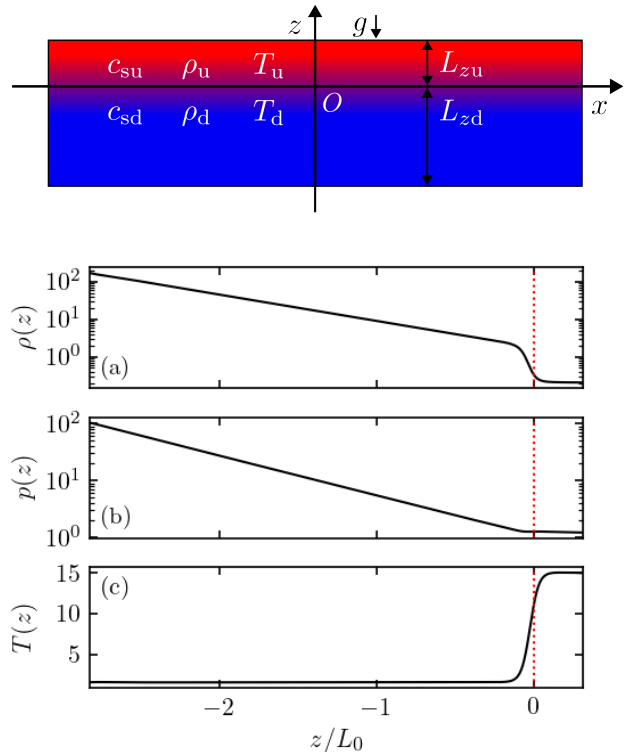


Figure 1. Top: Schematic of the the two-layer simulation domain. Bottom: Equilibrium profiles of (a) density, (b) pressure, and (c) temperature as a function of z for $L_z/L_0 = \pi$. The red dotted line marks the interface at $z = 0$.

We further assume a sharp discontinuity in the thermodynamic variables across the interface, as illustrated in bottom panel Figure 1. All the length scales are nondimensionalized using $L_0 = \gamma H_d = c_{sd}^2/g$, where H_d is the isothermal pressure scale height of the lower subdomain and c_{sd} is the adiabatic sound speed in the lower subdomain.

By assuming the conducting fluid to be ideal, we can write down the EOS as $p = (c_p - c_v)\rho T = \rho c_s^2/\gamma$, where p , ρ , T are respectively pressure, density and temperature, c_p and c_v are specific heat at constant pressure and volume, c_s is the adiabatic sound speed and $\gamma = c_p/c_v$ is the adiabatic index. In this work, both layers are taken to be isothermal. While there are other possibilities, we have not explored them here.

It would be interesting to investigate the effect of different kinds of layers and test the robustness of the results we discuss here.

Since gravity is constant and both layers are isothermal, in hydrostatic equilibrium, both layers are exponentially stratified as

$$\rho_{d,u}(z) = \rho_{d,u}(0) \exp\left(-\frac{z}{H_{d,u}}\right) \quad (1)$$

where $H_{d,u} = (c_p - c_v)T_{d,u}/g$ is the scale height of the lower and upper subdomains. Here, $\rho_d(0)$ and $\rho_u(0)$ are the densities at the interface, T_d and $T_u (> T_d)$ are the constant temperatures in the lower and upper subdomains, respectively. This defines our background state, on top of which perturbations are introduced.

This model can be regarded as a simplified representation of a small region of the Sun near its surface, with the interface mimicking the solar surface. The subdomain below the interface corresponds to the outer part of the convection zone, while the region above represents the solar atmosphere. This model, despite its simplicity, is sufficient for our purpose. A potential limitation is the use of an isothermal lower subdomain, whereas the solar convective zone is weakly superadiabatic. In future work, we will address this issue. For now, we adopt this simplified model, recognizing that it does not fully capture the thermodynamic structure of the solar interior.

2.2. Evolution equations

Having established the background state, we now describe the evolution equations used to excite the dynamo and the f -modes in our model. We solve the following set of equations

$$\frac{D \ln \rho}{Dt} = -\nabla \cdot \mathbf{u} \quad (2)$$

$$\frac{D \mathbf{u}}{Dt} = \mathbf{f} + \mathbf{g} + \frac{1}{\rho} (\mathbf{J} \times \mathbf{B} - \nabla P + \nabla \cdot 2\nu \rho \mathbf{S}) \quad (3)$$

$$T \frac{D s}{Dt} = 2\nu \mathbf{S}^2 + \frac{\mu_0 \eta}{\rho} \mathbf{J}^2 - \gamma(c_p - c_v) \frac{T - T_{d,u}}{\tau_{d,u}} \quad (4)$$

$$\frac{\partial \mathbf{A}}{\partial t} = \mathbf{u} \times \mathbf{B} - \mu_0 \eta \mathbf{J} \quad (5)$$

with appropriate boundary and initial conditions (discussed below). In the above equations, ρ is the density, \mathbf{u} is the velocity, and D/Dt denotes the convective time derivative. The term \mathbf{f} represents a forcing function, while $\mathbf{g} = (0, 0, -g)$ is the gravitational acceleration. The magnetic field is given by $\mathbf{B} = \nabla \times \mathbf{A}$, where \mathbf{A} is the vector potential, $\mathbf{J} = \mu_0^{-1}(\nabla \times \mathbf{B})$ is the current density. The pressure is denoted by p , and the traceless rate of strain tensor is defined as

$$S_{ij} = \frac{1}{2}(u_{i,j} + u_{j,i}) - \frac{1}{3}\delta_{ij}\nabla \cdot \mathbf{u}, \quad (6)$$

where commas denote partial differentiation. The specific entropy is denoted by s , the temperature by T , and μ_0 represents the vacuum permeability. The kinematic viscosity ν and magnetic diffusivity η are taken to be constants. Finite values of ν and η are included primarily to ensure numerical stability. These parameters are chosen to be sufficiently small so as not to affect the f -mode dynamics, while remaining large enough to suppress grid-scale instabilities. We find that values $\nu, \eta \sim 10^{-3}-10^{-4}$ are sufficient for our purposes.

The set of equations (2)-(5) constitutes an almost standard set of MHD equations, extended to serve our specific purpose. The inclusion of the relaxation term in equation (4) can be motivated as follows. The presence of finite ν and η in the evolution equations will lead to the conversion of kinetic and magnetic energy to thermal energy, which would otherwise heat the background state. To counteract this effect, we introduce a relaxation term that maintains the prescribed background stratification. This approach is motivated by [Singh et al. \(2015\)](#). While they applied this term only in the upper subdomain, we found that in our 3D setup, it is necessary to include it in both subdomains. Without the relaxation term in the lower subdomain, the upper subdomain gradually heats the lower one, thereby reducing the sharpness of the interface. Since a well-defined interface is crucial for excitation of the f -mode, incorporating the relaxation term in both subdomains is essential. Thus, for the upper layer, we choose a relaxation rate $\tau_u^{-1} = 0.45 \text{ g}/\text{c}_{\text{sd}}$, while for the lower layer we adopt $\tau_d^{-1} = 0.25 \text{ g}/\text{c}_{\text{sd}}$ throughout this paper.

Our background state is static, so to introduce perturbations, we have included a stochastic forcing term ([Brandenburg \(2001\)](#)) in the equation (3). This term serves two purposes: it introduces small perturbations into the background state in an isotropic and homogeneous manner at a length scale smaller than the box size, thereby exciting various modes; second, the forcing is chosen to be helical, injecting kinetic helicity into the flow and breaking mirror symmetry, which is a necessary condition for large-scale dynamo action. Since we aim to excite the dynamo primarily in the lower layer, the forcing is set to zero in the upper layer.

The average forcing wavelength k_f defines the energy injection scale $l_f = 2\pi/k_f$. The smallest wavenumber in the system is $k_1 = 2\pi/\max(L_x, L_y, L_z) = 2\pi/L_x$, which in our setup corresponds to $k_1 = 2\pi/L_x$. For the box size used in this work, we obtain $k_f/k_1 \approx 56$.

2.3. Boundary conditions

We apply periodic boundary conditions for all eight variables at the boundaries in the horizontal direction. However, in the stratified vertical z direction, we impose physically motivated boundary conditions at the top and bottom. For velocity, we choose the free slip condition to avoid the emergence of boundary layers, which are unimportant in an

astrophysical context. For the entropy equation, we fix the temperature at both boundaries, while for density, we set its second derivative to zero at the boundaries. For the magnetic field, we apply perfectly conducting boundary conditions at both the top and bottom.

2.4. Initial conditions

We set the initial velocity to zero throughout the domain. For the density, we prescribe the two-layer profile shown in the panel (a) of Figure 1 (bottom). Using density and temperature profiles together with the fundamental thermodynamic relations, we compute the corresponding entropy profile for our background state and prescribe it as the initial condition for the entropy, in a manner analogous to density. Finally, for the magnetic field, we assume a normally distributed white noise of small amplitude as the initial seed magnetic field.

2.5. Software

All simulations were performed using the PENCIL CODE¹ (Pencil Code Collaboration et al. 2021), a publicly available high-order finite-difference code for weakly compressible magnetohydrodynamics.

All the analyses were carried out using publicly available Python packages, including MATPLOTLIB (Hunter 2007), NUMPY (van der Walt et al. 2011), SCIPY (Virtanen et al. 2020).

3. METHODOLOGY

To investigate the effect of the magnetic field on f -mode, we use one of the fundamental tools of helioseismology (Gizon & Birch 2005): k - ω diagram. For our setup, calculating the k - ω diagram from simulated data is straightforward and analogous to its observational counterpart (essentially the same). We save 2D snapshots of the vertical velocity component $u_z(t, x, y, z = 0)$ at the interface ($z = 0$) at regular time intervals, analogous to Dopplergrams in observations. The snapshots are stacked sequentially to form a 3D data cube. We then perform the Fourier transform along all three axes to obtain $\hat{u}_z(\omega, k_x, k_y)$. The corresponding energy spectral density is given by $P(\omega, k_x, k_y) = |\hat{u}_z|^2$. Finally, to construct the k - ω diagram, we may choose either $k_y = 0$ or $k_x = 0$. In all results presented below, we adopt $k_y = 0$.

The results are presented in terms of dimensionless quantities. This is not strictly necessary for the present study since all the relevant physical parameters are identical for all the runs. Still, we have adopted this normalization for consistency and to facilitate potential future follow-up work. Specifically, we use the same normalization as discussed in Singh et al. (2015):

$$\tilde{k}_x = k_x L_0, \quad \tilde{\omega} = \frac{\omega}{\omega_0}, \quad (7)$$

where $L_0 = \gamma H_d = c_{\text{sd}}^2/g$ and $\omega_0 = g/c_{\text{sd}}$ represents the inverse of the characteristic timescale for acoustic wave propagation in a stratified medium. Remembering that \hat{u}_z has the dimension of $[LT^{-1}]$, we non-dimensionalize the power spectrum as

$$\tilde{P} = \frac{P}{c_{\text{sd}}^2} = \left(\frac{|\hat{u}_z|}{c_{\text{sd}}} \right)^2 = \left(\frac{|\hat{u}_z|}{L_0 \omega_0} \right)^2. \quad (8)$$

where, c_{sd} is the adiabatic sound speed of the lower sub-domain. Thus, \tilde{P} is simply the squared Mach number of vertical velocity component in Fourier space.

3.1. Mode fitting

To quantify the behavior of the f -mode, we extract the power spectrum $\tilde{P}_{\tilde{k}_x}(\tilde{\omega})$ as a function of $\tilde{\omega}$ for different \tilde{k}_x . Each profile is then fitted using a Lorentzian function to represent the mode and a linear function to model the background continuum. Therefore, the fitting function we use is of the following form

$$\tilde{P}_{\tilde{k}_x}(\tilde{\omega}) = \sum_i \frac{A_i \Gamma_i / \pi}{(\tilde{\omega} - \tilde{\omega}_{c,i})^2 + \Gamma_i^2} + B \tilde{\omega} + C \quad (9)$$

where A_i , $\tilde{\omega}_{c,i}$, Γ_i denote the amplitude, central frequency, and linewidth of the i th mode, respectively, while B and C characterize the background. The choice of a linear background is not motivated by any theoretical reasoning but rather by empirical observations from the dataset. For the fitting procedure, we employ SciPy's `curve_fit` function, which provides reliable and accurate results.

For low \tilde{k}_x , where f and p -modes are closely spaced in frequency (see Figure 2 and Figure 4), we therefore fit them simultaneously assuming a Lorentzian profile for each of them. At larger \tilde{k}_x , where modes are well separated, only the f -mode and the background are fitted.

To characterize the f -mode, we adopt three diagnostic parameters proposed by Singh et al. (2015), evaluated at fixed \tilde{k}_x from the Lorentzian profile obtained after subtracting the linear background from $\tilde{P}_{\tilde{k}_x}(\tilde{\omega})$. The first is the relative frequency shift, defined as

$$\left(\frac{\delta \omega_f^2}{\omega_f^2} \right) (\tilde{k}_x) = \frac{\omega_{cf}^2 - \omega_f^2}{\omega_f^2}, \quad (10)$$

where ω_f is the theoretical frequency from equation (13), and ω_{cf} is the fitted line-center frequency of the f -mode. This parameter quantifies the shift of the line center relative to its theoretical value.

To quantify the amplitude of the f -mode, we define mode strength μ_f as the integrated excess energy in the mode frequency range:

$$\mu_f(\tilde{k}_x) = \int \Delta \tilde{P}_{\tilde{k}_x}(\tilde{\omega}) d\tilde{\omega}, \quad (11)$$

¹ <https://pencil-code.nordita.org/>

where $\Delta\tilde{P}_{\tilde{k}_x}(\tilde{\omega})$ represents the normalized energy excess over the continuum of the f -mode. This quantity serves as a proxy for the kinetic energy of the mode.

Finally, the relative linewidth is quantified using the dimensionless parameter

$$\Gamma_f(\tilde{k}_x) = \frac{\Delta\omega_{\text{FWHM}}}{\omega_{\text{cf}}}, \quad (12)$$

where $\Delta\omega_{\text{FWHM}}$ is the full width at half maximum (FWHM) of the fitted line profile. Note that this relative linewidth is the inverse of the standard quality factor Q .

4. RESULTS

To study how a dynamo-generated large-scale magnetic field affects the f -mode, we performed two simulations in total. One of them, labeled h1, is a purely hydrodynamic case. The other run, d1, is hydromagnetic. Both simulations were carried out at the same grid resolution of $1024 \times 256 \times 320$, with identical physical parameters across the runs. The computational domain has dimensions $12\pi \times 3\pi \times \pi$ (in units of L_0) and a constant kinematic viscosity $\nu = 0.001$. For the magnetic case (d1), we additionally employ a constant magnetic diffusivity $\eta = 0.001$. These choices corresponds to an approximate Reynolds number of $Re \approx 18$, and a magnetic Prandtl number $P_m = 1$ in the hydromagnetic simulations.

4.1. Non-magnetic case

Before turning into the magnetic case, we first discuss the wave modes in the purely hydrodynamic run h1. The k - ω diagram for this run is shown in Figure 2. The k - ω diagram reveals the excitation of both the f -mode and several p -modes in the domain. For a two-layer isothermal setup as ours, four critical lines exist in the k - ω diagram. Of these, we show two: $\omega = c_{\text{su}}k_h$ (dashed line) and $\omega = c_{\text{sd}}k_h$ (solid line). The remaining two critical lines (not shown) are $\omega = N_u$ and $\omega = N_d$, where N_u and N_d are the Brunt-Väisälä (Stein & Leibacher 1974) frequencies of the upper and lower layers, respectively.

Since our primary interest in this work is the f -mode, we briefly summarize its theoretical properties. The f -mode is a surface gravity wave that exists due to a discontinuity in the density profile. For our model, the dispersion relation of the f -mode can be calculated analytically (Lamb 1932) and is given by

$$\omega_f^2 = \omega_{f0}^2 \frac{1-q}{1+q}, \quad \omega_{f0}^2 = gk_h, \quad (13)$$

where k_h is the horizontal wavenumber; for the present purpose, $k_h = k_x$. The parameter q is defined as

$$q = \frac{\rho_u(0)}{\rho_d(0)} = \frac{c_{\text{sd}}^2}{c_{\text{su}}^2} = \frac{H_d}{H_u} = \frac{T_d}{T_u}, \quad (14)$$

and characterizes the jump in the thermodynamic variables across the interface at $z = 0$. Here, ω_{f0} denotes the angular frequency of the f -mode in the limit $q \rightarrow 0$. The dashed and solid curves in Figure 2 show ω_{f0} and ω_f , respectively.

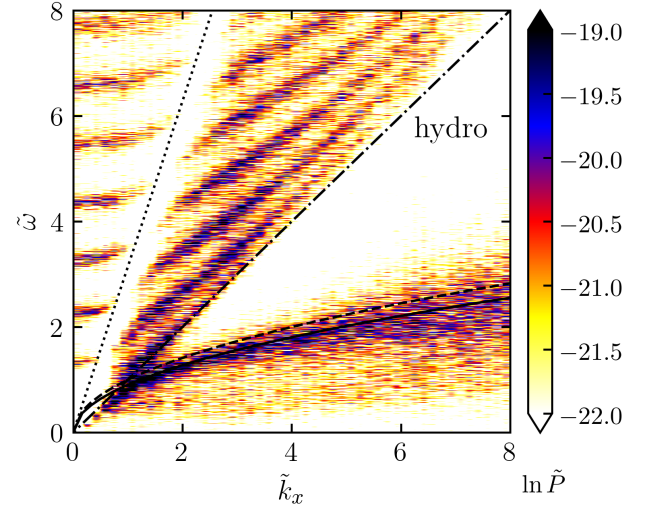


Figure 2. k - ω diagram for the non-magnetic run h1. The dotted and dot-dashed lines show $\tilde{\omega} = c_{\text{su}}\tilde{k}_x$ and $\tilde{\omega} = c_{\text{sd}}\tilde{k}_x$ respectively. The dashed and solid curves show $\tilde{\omega}_{f0}$ and $\tilde{\omega}_f$ respectively.

For the low value of \tilde{k}_x , f -mode frequencies lie close to the ω_f curve, whereas for large \tilde{k}_x , they deviate from it and the mode also broadens. Such broadening can be attributed to the turbulent nature of the flow (Mędryk et al. 1999; Murawski 2000).

To facilitate comparison, we present the variation of all three mode parameters (discussed above) in the next section (see Figure 5) alongside the corresponding values obtained from the hydromagnetic run.

4.2. With α^2 dynamo

We begin by examining the evolution of the magnetic field itself, before turning to the behavior of the f -mode in the presence of magnetic fields. As mentioned above, we incorporate an α^2 dynamo (Brandenburg & Subramanian 2005) in the lower subdomain, where an initial weak seed magnetic field is amplified through the dynamo action. Figure 3a shows the time evolution of the kinetic and magnetic energies for the hydromagnetic run d1. Time is expressed in units of eddy turnover time $\tau_{\text{edd}} = 1/(u_{\text{rms},d} k_f)$, where $u_{\text{rms},d}$ is the rms velocity measured in the lower layer. Since the dynamo operates only in the lower layer, this definition appropriately characterizes the relevant dynamical timescale. The growth of the magnetic energy exhibits an initial exponential phase, indicative of the kinematic dynamo regime, followed by a transitional phase and eventual saturation at later times. In the saturated phase, the magnetic field reaches an

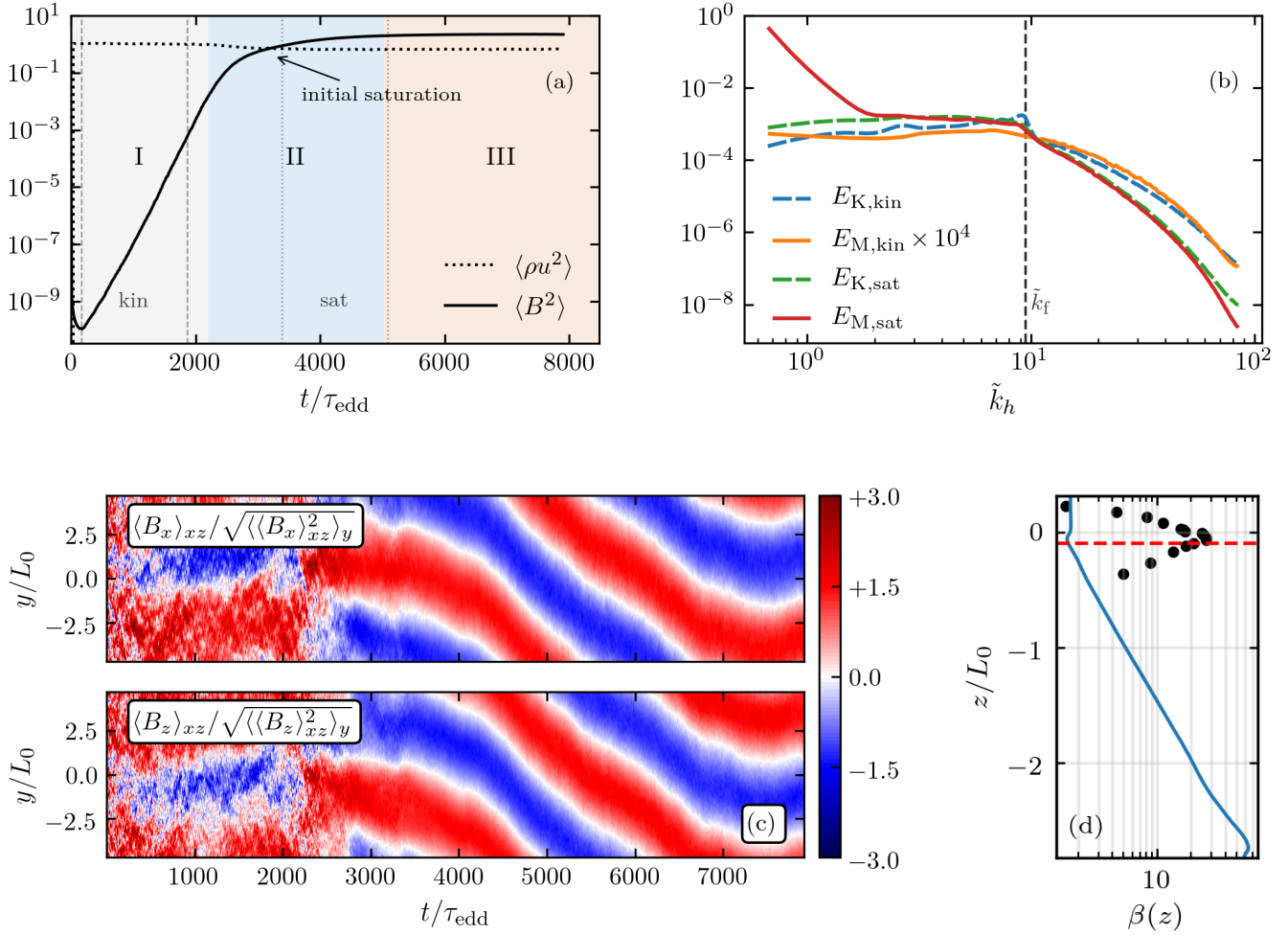


Figure 3. (a) Time evolution of the kinetic and magnetic energies for run d1. Three phases, (I) kinematic, (II) weak nonlinear, and (III) saturated, of the α^2 dynamo are highlighted. (b) Kinetic and magnetic energy spectra are shown from the plane at $z = -0.1L_0$, during the kinematic and saturated phases. Black dashed line shows the forcing wavenumber k_f . (c) Space-time diagram of the mean magnetic field components. Magnetic fields are first averaged over the x - z plane to define $\langle B_x \rangle_{xz}$ and $\langle B_z \rangle_{xz}$. These quantities are then normalized by their corresponding rms values $\sqrt{\langle \langle B_x \rangle_{xz}^2 \rangle_y}$ and $\sqrt{\langle \langle B_z \rangle_{xz}^2 \rangle_y}$, respectively. (d) Vertical profile of horizontally averaged plasma beta $\beta(z)$, in the saturated phase. Black circles show the eigenfunction of the f -mode near the free surface, scaled by a factor of 10^{10} for clarity. The red dashed line marks $z = -0.1L_0$.

rms strength of $B_{\text{rms}} = 1.4 B_{\text{eq}}$, where the equipartition field is defined as $B_{\text{eq}} = (\mu_0 \rho_{\text{d}} u_{\text{rms},\text{d}}^2)^{1/2}$.

We select two representative time intervals, one from the kinematic phase and another from the post-equipartition stage to examine how a dynamically evolving magnetic field influences the f -mode. These intervals are marked in the Figure 3a. For the kinematic phase, we consider the data between the dashed vertical lines (hereafter *kin*), while for the post-equipartition stage (hereafter *sat*) we consider the data between the dotted vertical lines.

The Figure 3b shows various two-dimensional energy spectra at $z = -0.1 L_0$, which is the same depth used to construct the k - ω diagrams analyzed below. Although the kinetic energy spectrum for the non-magnetic run h1 is not

shown here, it is identical to $E_{K,\text{kin}}$, as expected. Two main observations can be made from this figure.

First, the excitation of the α^2 dynamo is evident. We find that the magnetic energy in the kinematic phase ($E_{M,\text{kin}}$) is approximately 10^{-4} times smaller than that in the saturated phase ($E_{M,\text{sat}}$). Moreover, $E_{M,\text{sat}}$ peaks near the largest scale of the box, as expected.

Second, we observe that the kinetic energy shifts from smaller scales to larger scales as the dynamo saturates. This increase in kinetic energy at large scales can, in turn, strengthen different modes. Below, we confirm that this is indeed the case.

Figure 3c shows the space-time diagrams of the different mean magnetic field components for run d1, illustrating the

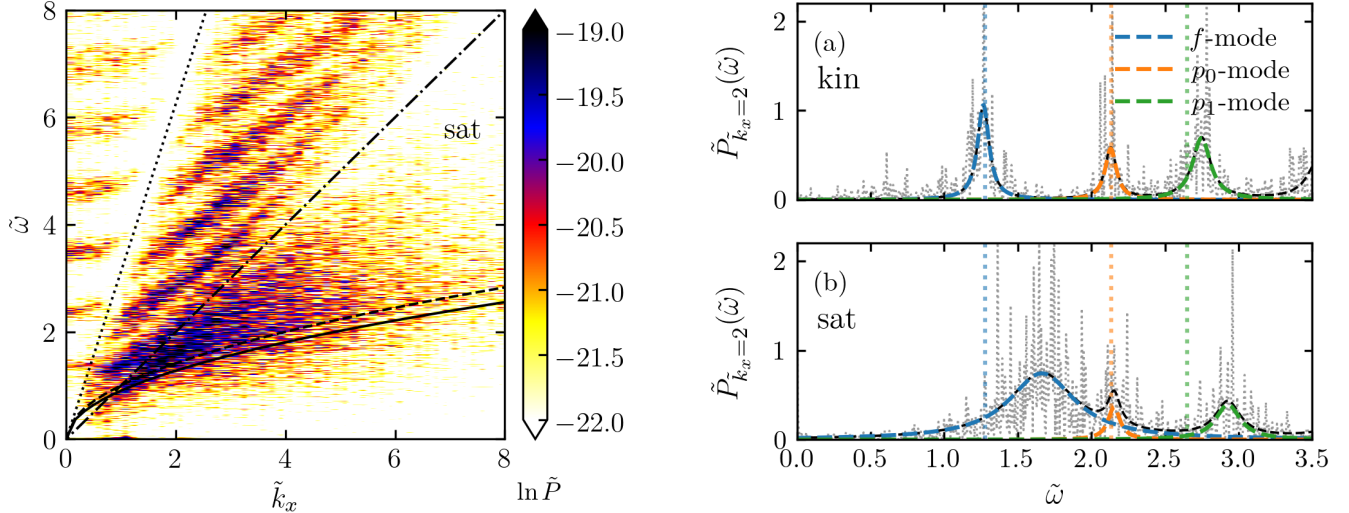


Figure 4. Left: Same as Figure 2 but for the magnetic run d1. A noticeable broadening of the f -mode is seen with increasing \tilde{k}_x . Right: Line profiles of the f , p_0 , and p_1 -mode at $\tilde{k}_x = 2$ for the kinematic phase (panel a) and for the saturated phase (panel b); dotted curves represent the data. To ensure a consistent comparison, the background has been removed. Blue dashed lines show the locations of the f -mode.

evolution of the magnetic-field structure in our box. The field evolves from an initially noisy state to large-scale dynamo waves, exhibiting typical α^2 dynamo behavior.

Figure 3d shows the horizontally averaged plasma beta $\beta(z)$ for the saturated phase, with black circles indicating the f -mode eigenfunction near the interface ($z = 0$). In our setup, the f -mode decays exponentially on both sides of $z = 0$. The small values of β near the interface suggest that magnetic pressure dominates within the f -mode cavity.

Having established the presence and the evolution of dynamo in our simulation, we now turn to the wave dynamics of the system, focusing on the k - ω diagram and the f -mode. Our approach is straightforward: By analyzing the power spectrum of vertical velocity fluctuations at the interface, we identify the characteristic signatures of different wave modes and assess how they are influenced by the dynamo-generated magnetic fields. Figure 4 (left) shows the k - ω diagram for the saturated phase of the run d1; the k - ω diagram for the kinematic phase is not shown here, but it is similar to the non-magnetic case (Figure 2). We use the same data length for the kinematic and saturated intervals marked in Figure 3a to ensure a consistent comparison.

Examining the k - ω diagrams, we observe that in the saturated phase, the f -mode undergoes significant broadening, consistent with previous studies (Singh et al. 2014). To investigate this in more detail, we analyze the power spectrum at different values of \tilde{k}_x . Figure 4 (right) presents a representative example. In the figure, we show the dimensionless spectral mode amplitude $\tilde{P}_{\tilde{k}_x=2}(\tilde{\omega})$ at $\tilde{k}_x = 2$ as a black dotted curve. Panel (a) corresponds to the kinematic phase, and panel (b) to the saturated phase. In both panels, three distinct peaks are visible, corresponding to the f , p_0 , and p_1 modes

from left to right. The fitted Lorentzian profiles are overplotted: blue for the f -mode, orange for the p_0 -mode, and green for the p_1 -mode.

In the kinematic phase [panel (a)], each mode is fitted separately and shown here for completeness. In contrast, in the saturated phase [panel (b)], the f -mode broadens significantly and partially merges with the p_0 and p_1 modes, particularly at low \tilde{k}_x . Therefore, all three modes are fitted together in this case. The combined fit is shown as a black dashed curve in panel (b), clearly capturing the broadened nature of the f -mode.

From the fitted profiles of the f -mode for two different phases, we calculate three mode parameters prescribed in section 3.1 for various \tilde{k}_x and for different runs. Figure 5 summarizes our results. The parameters for the non-magnetic case are shown by black triangles, while circular (red) and square markers (blue) denote the kinematic and saturated phases, respectively.

From Figure 5, we observe that f -mode characteristics calculated from the non-magnetic case (h1) and the kinematic phase of magnetic run d1 are identical. This behavior is evident in all three panels, indicating that the kinematic phase of a dynamo effectively acts as a non-magnetic case.

What particularly striking, however, is the behavior of the f -mode in the saturated phase of the dynamo. Panel (a) shows a clear enhancement of the f -mode strength indicating a strengthening of the f -mode. During the kinematic phase, the dynamo converts kinetic energy to magnetic energy, leading to the growth of the magnetic field. Once magnetic energy becomes comparable to the kinetic energy, the magnetic field begins to influence the flow through the Lorentz force. This feedback quenches the fluid flow, and

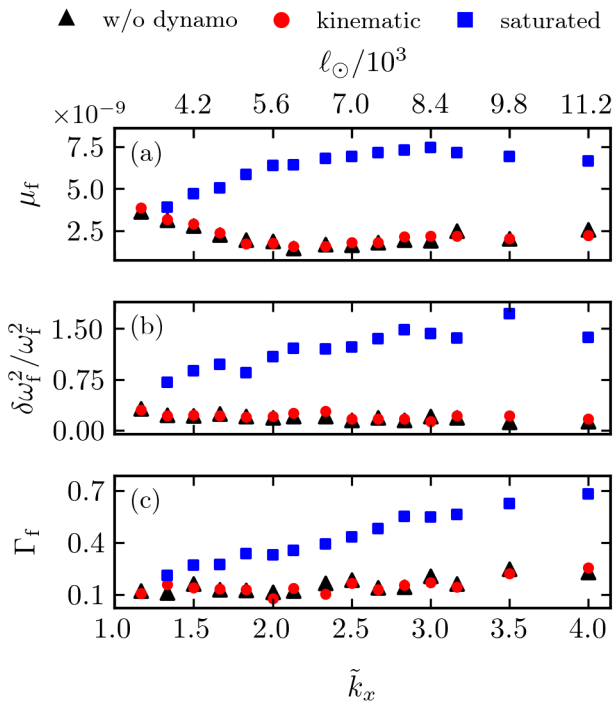


Figure 5. Variation of different f -mode characteristics with \tilde{k}_x for different runs. (a) Mode strength (μ_f), (b) relative frequency shift, and (c) full width at half maximum (FWHM) of the f -mode, all as functions of \tilde{k}_x . Tick marks at the top indicate the corresponding spherical harmonic degree ℓ .

through the non-linear interaction, the magnetic field saturates to a finite amplitude. This quenching of the fluid flow results in a reduction of the system's kinetic energy. Naively, this reduction would suggest a corresponding decrease in the mode strength. However, our results reveal that the interaction between the dynamically evolving large-scale magnetic field and the f -mode instead leads to its strengthening. This enhancement is directly proportional to the magnitude of the magnetic field near the interface, where the f -mode is primarily localized.

In addition to the increase in mode strength, we also observe the other well-known effects of the magnetic field on f -mode. Panel (b) shows that the magnetic field shifts the f -mode frequency, with the magnitude of the shift increasing with wavenumber. Panel (c) further demonstrates that the FWHM of the f -mode exhibits a similar trend. In the hydrodynamic case, we also observe f -mode broadening, which we attribute to the turbulent nature of the flow. The linewidths in the kinematic phase of d1 run (red circles) closely match those of the hydrodynamic case. In contrast, in the saturated phase, the broadening is significantly larger. Such broadening of f -mode was first reported by Singh et al. (2014), who referred to it as a 'fanning out' of the f -mode

and attributed it to the nonuniform nature of the magnetic field.

Throughout this section, our results have been presented in terms of the nondimensional wavenumber \tilde{k}_x . To assess their observational relevance, it is useful to relate \tilde{k}_x with the spherical harmonic degree ℓ . To do so, we recall that $\tilde{k}_x = k_x L_0$, where $L_0 = \gamma H_d$. For the Sun, we approximate this by choosing $\gamma \sim 5/3$ and $H_d = H_\odot \sim 0.15$ Mm, which is roughly the scale height near the photosphere. Hence, the corresponding wavenumber for the Sun is given by $k \sim \tilde{k}_x / (\gamma H_\odot)$, where $\gamma H_\odot \sim 0.25$ Mm. This leads to the relation $\ell \sim \tilde{k}_x R_\odot / (\gamma H_\odot) \sim 2800 \tilde{k}_x$. Using this relation, the corresponding spherical harmonic degree ℓ for each value of \tilde{k}_x is shown along the top of the axis of Figure 5. This mapping implies that the effects identified in this study are expected to manifest at relatively high ℓ compare to those accessible in current observations. However, we note that the isothermal stratification of the bulk as adopted in this study is too idealistic and this leads to an overlap of the f and p modes for $k_x \lesssim 1$. It is therefore likely that the effects as seen in this work would continue to be relevant for the lower ℓ 's in a more realistic polytropic bulk which will be explored in a separate study.

From the k - ω diagrams as shown in Figs 2 and 4, and visually comparing the p -mode ridges, we find that the p -modes too are relatively more broadened and their frequencies are higher when the magnetic fields saturate in the dynamo run as compared to the purely hydrodynamic case. Further investigations on the properties of p -modes in presence of dynamo generated magnetic fields will be taken up elsewhere.

5. CONCLUSIONS

Previous studies of this kind suffer from the objection that they often impose magnetic fields by hand with arbitrary magnitudes. Here, in this work, we relax this by including an α^2 -dynamo in the lower subdomain of the box, allowing the magnetic field to evolve on its own. We found that the kinematic phase of such a dynamo run effectively acts as a non-magnetic case. All three f -mode parameters namely, the mode strength, frequency shift and linewidth for the kinematic phase are almost the same as those obtained from the non-magnetic run h1. This is expected as, in the kinematic phase, the magnetic field is too weak to affect the velocity field; hence, the characteristics of f -mode are the same in both cases.

But as the dynamo evolves and generates large-scale magnetic fields, it begins to interact with the velocity field, thereby affecting the f -mode. We find that the magnetic field not only increases the frequency of the f -mode, but also strengthens it and fans it out, which is clearly noticeable in the k - ω diagram (see Figure 4). This increase in the mode strength depends on the magnitude of the mag-

netic field near the surface, with these effects being more pronounced at larger wavenumbers.

One possible caveat in this and other similar works with isothermal stratification in the bulk is that the f and p modes overlap and interfere with each other for $\tilde{k}_x \lesssim 1$, i.e., for $\ell \lesssim 2800$. This limits our ability to explore the regime where current observations are more sensitive. To address this, one needs to consider more realistic polytropic stratification for the bulk. This will be taken up in a future study.

6. ACKNOWLEDGMENTS

All simulations were performed on the Pegasus cluster at IUCAA. We sincerely acknowledge the computing facilities provided by IUCAA. We thank Kishore Gopalakrishnan for valuable discussions and insights.

REFERENCES

Brandenburg, A. 2001, *ApJ*, 550, 824, doi: [10.1086/319783](https://doi.org/10.1086/319783)

Brandenburg, A., & Subramanian, K. 2005, *PhR*, 417, 1, doi: <https://doi.org/10.1016/j.physrep.2005.06.005>

Cally, P. S., & Bogdan, T. J. 1997, *ApJL*, 486, L67, doi: [10.1086/310833](https://doi.org/10.1086/310833)

Chandrasekhar, S. 1961, *Hydrodynamic and Hydromagnetic Stability* (Oxford University Press)

Christensen-Dalsgaard, J. 2002, *Rev. Mod. Phys.*, 74, 1073, doi: [10.1103/RevModPhys.74.1073](https://doi.org/10.1103/RevModPhys.74.1073)

Daifallah, K., Abdelfatif, T., Bendib, A., Cameron, R., & Gizon, L. 2011, *SoPh*, 268, 309, doi: [10.1007/s11207-010-9666-5](https://doi.org/10.1007/s11207-010-9666-5)

Erdélyi, R., Kerekes, A., & Mole, N. 2005, *A&A*, 431, 1083, doi: [10.1051/0004-6361:20041456](https://doi.org/10.1051/0004-6361:20041456)

Felipe, T., Braun, D., Crouch, A., & Birch, A. 2012, *ApJ*, 757, 148, doi: [10.1088/0004-637X/757/2/148](https://doi.org/10.1088/0004-637X/757/2/148)

Gizon, L., & Birch, A. C. 2005, *Living Reviews in Solar Physics*, 2, 6, doi: [10.12942/lrsp-2005-6](https://doi.org/10.12942/lrsp-2005-6)

Hanasoge, S. M., Birch, A. C., Bogdan, T. J., & Gizon, L. 2008, *ApJ*, 680, 774, doi: [10.1086/587455](https://doi.org/10.1086/587455)

Hunter, J. D. 2007, *Computing in Science and Engineering*, 9, 90, doi: [10.1109/MCSE.2007.55](https://doi.org/10.1109/MCSE.2007.55)

Kasapis, S., Kitiashvili, I. N., Kosovichev, A. G., & Stefan, J. T. 2024, arXiv e-prints, arXiv:2409.17421, doi: [10.48550/arXiv.2409.17421](https://doi.org/10.48550/arXiv.2409.17421)

Kasapis, S., Dogan, E., Kitiashvili, I. N., et al. 2026, arXiv e-prints, arXiv:2601.13145, doi: [10.48550/arXiv.2601.13145](https://doi.org/10.48550/arXiv.2601.13145)

Kiefer, R., Schad, A., & Roth, M. 2017, *ApJ*, 846, 162, doi: [10.3847/1538-4357/aa8634](https://doi.org/10.3847/1538-4357/aa8634)

Kishore, G., Singh, N. K., Käpylä, P., & Roth, M. 2024, arXiv e-prints, arXiv:2409.14840, doi: [10.48550/arXiv.2409.14840](https://doi.org/10.48550/arXiv.2409.14840)

Korpi-Lagg, M. J., Korpi-Lagg, A., Olspert, N., & Truong, H. L. 2022, *A&A*, 665, A141, doi: [10.1051/0004-6361/202243979](https://doi.org/10.1051/0004-6361/202243979)

Lamb, H. 1932, *Hydrodynamics*

Mędryk, M., Murawski, K., & Roberts, B. 1999, *A&A*, 349, 312

Miles, A. J., Allen, H. R., & Roberts, B. 1992, *SoPh*, 141, 235, doi: [10.1007/BF00155177](https://doi.org/10.1007/BF00155177)

Miles, A. J., & Roberts, B. 1989, *SoPh*, 119, 257, doi: [10.1007/BF00146179](https://doi.org/10.1007/BF00146179)

—. 1992, *SoPh*, 141, 205, doi: [10.1007/BF00155176](https://doi.org/10.1007/BF00155176)

Murawski, K. 2000, *A&A*, 360, 707

Parchevsky, K. V., & Kosovichev, A. G. 2009, *ApJ*, 694, 573, doi: [10.1088/0004-637X/694/1/573](https://doi.org/10.1088/0004-637X/694/1/573)

Pencil Code Collaboration, Brandenburg, A., Johansen, A., et al. 2021, *The Journal of Open Source Software*, 6, 2807, doi: [10.21105/joss.02807](https://doi.org/10.21105/joss.02807)

Roberts, B. 1981, *SoPh*, 69, 27, doi: [10.1007/BF00151253](https://doi.org/10.1007/BF00151253)

Singh, N. K., Brandenburg, A., Chitre, S. M., & Rheinhardt, M. 2015, *MNRAS*, 447, 3708, doi: [10.1093/mnras/stu2540](https://doi.org/10.1093/mnras/stu2540)

Singh, N. K., Brandenburg, A., & Rheinhardt, M. 2014, *ApJL*, 795, L8, doi: [10.1088/2041-8205/795/1/L8](https://doi.org/10.1088/2041-8205/795/1/L8)

Singh, N. K., Raichur, H., & Brandenburg, A. 2016, *ApJ*, 832, L8, doi: [10.3847/2041-8205/832/1/L8](https://doi.org/10.3847/2041-8205/832/1/L8)

Singh, N. K., Raichur, H., Käpylä, M. J., et al. 2020, *Geophysical and Astrophysical Fluid Dynamics*, 114, 196, doi: [10.1080/03091929.2019.1653461](https://doi.org/10.1080/03091929.2019.1653461)

Stein, R. F., & Leibacher, J. 1974, *ARA&A*, 12, 407, doi: [10.1146/annurev.aa.12.090174.002203](https://doi.org/10.1146/annurev.aa.12.090174.002203)

Thompson, M. J. 2006, *Philosophical Transactions: Mathematical, Physical and Engineering Sciences*, 364, 297, <http://www.jstor.org/stable/25190191>

Tripathi, B., & Mitra, D. 2022, *ApJ*, 934, 61, doi: [10.3847/1538-4357/ac79b1](https://doi.org/10.3847/1538-4357/ac79b1)

van der Walt, S., Colbert, S. C., & Varoquaux, G. 2011, *Computing in Science and Engineering*, 13, 22, doi: [10.1109/MCSE.2011.37](https://doi.org/10.1109/MCSE.2011.37)

Virtanen, P., Gommers, R., Oliphant, T. E., et al. 2020, *Nature Methods*, 17, 261, doi: [10.1038/s41592-019-0686-2](https://doi.org/10.1038/s41592-019-0686-2)

Waidele, M., Roth, M., Singh, N., & Käpylä, P. 2023, *SoPh*, 298,